

Article

Optimal Escape from Sun-Earth and Earth-Moon L2 with Electric Propulsion

Luigi Mascolo [†]  and Lorenzo Casalino ^{*,†} 

Dipartimento di Ingegneria Meccanica e Aerospaziale, Politecnico di Torino, Corso Duca degli Abruzzi, 24, 10129 Torino, Italy; luigi.mascolo@polito.it

* Correspondence: lorenzo.casalino@polito.it

† These authors contributed equally to this work.

Abstract: Optimal low-thrust trajectories for the direct escape from the Earth's sphere of influence, starting from Sun-Earth or Earth-Moon L2, are analyzed with an indirect optimization method. The dynamic model considers four-body gravitation and JPL ephemeris; solar radiation pressure is also considered. Specific techniques and improvements to the method are introduced to tackle the highly chaotic and nonlinear dynamics of motion close to Lagrangian points, which challenges the remarkable precision of the indirect method. The results show that escape trajectories have optimal performance when the solar perturbation acts favorably in both thrust and coast phases. The effects of the solar and Moon perturbations are more evident in the Earth-Moon L2 escapes compared with those from the Sun-Earth L2. EML2 escapes have single- or two-burn solutions depending on the trajectory deflection, which is needed to have a favorable solar perturbation. The SEL2 escapes, on the contrary, mainly have a single initial burn and a long coast arc, but need an additional final thrust arc if the required C_3 is high. As applications of such Lagrangian Point trajectories, results include considerations about escape maneuvers from different SEL2 high-fidelity Lyapunov orbits and escape for interplanetary trajectories towards near-earth asteroids.

Keywords: escape trajectories; Lagrangian points; electric propulsion; trajectory optimization; indirect methods



Citation: Mascolo, L.; Casalino, L. Optimal Escape from Sun-Earth and Earth-Moon L2 with Electric Propulsion. *Aerospace* **2022**, *9*, 186. <https://doi.org/10.3390/aerospace9040186>

Academic Editor: Fabrizio Piergentili

Received: 29 January 2022

Accepted: 18 March 2022

Published: 1 April 2022

Publisher's Note: MDPI stays neutral with regard to jurisdictional claims in published maps and institutional affiliations.



Copyright: © 2022 by the authors. Licensee MDPI, Basel, Switzerland. This article is an open access article distributed under the terms and conditions of the Creative Commons Attribution (CC BY) license (<https://creativecommons.org/licenses/by/4.0/>).

1. Introduction

Lagrangian points (LPs) have received great interest in the last few decades. LPs represent equilibrium positions in the three-body dynamics, and a spacecraft at an LP remains locked in the reference frame (RF) which rotates with the two primaries (e.g., Sun and Earth or Earth and Moon), maintaining a fixed position [1]. In addition to these peculiar dynamical characteristics, these positions offer highly advantageous strategic locations for both logistic purposes and the study and analysis of deep space [2–7]. For these reasons, the scientific community is showing great interest in visiting LPs and, in the near future, numerous space missions are planned towards these points.

Among other initiatives, the European Space Agency is planning a mission [8] (formerly known as LAGRANGE) with two spacecraft in Sun-Earth L1 and L5 for observation and monitoring of interplanetary space and solar activity, and the PLATO mission [9], in Sun-Earth L2 (SEL2). In addition to being targets of specific missions, LPs could also be used as departure points for interplanetary missions. For instance, a recent contribution [10] showed how departures from either Sun-Earth L4 or Sun-Earth L5 might be extremely favorable for missions to near-earth asteroids (NEAs) that have small minimum orbit intersection distance (MOID), in particular when the target asteroid passes relatively close to the Earth.

In a similar way, the future Lunar Orbital Platform Gateway (LOP-G; formerly named Deep Space Gateway—DSG) is a joint effort led by NASA, in collaboration with CSA, ESA, and JAXA, in order to place a platform close to the Moon, on a stable orbit around, though

quite far from, Earth-Moon L2 (EML2). This orbiting platform will be used to greatly simplify some deep space operations, produce a more practical handling of lunar resources, and serve as a supply point for spacecraft, such as Deep Space Transport, moving to and from distant destinations [11–13]. NASA published a reference trajectory in the full ephemeris model for a 15-year-long positioning [14] of the LOP-G. The selected orbit is a southern L2 near rectilinear halo orbit (NRHO) with 9:2 lunar synodic resonance, which minimizes the required station-keeping maneuvers while eliminating eclipses almost completely.

Very small propulsive requirements (ΔV below 100 m/s and often even below 10 m/s) are needed to escape from LPs on low energy trajectories with final C_3 ($C_{3,f}$) below 0.5 (km/s)^2 ; these values are suitable, for instance, for missions to NEAs. These kinds of trajectories are the focus of the present paper, which aims at an initial evaluation of escape from SEL2 and EML2 for an electric propulsion (EP) spacecraft.

The optimization of EP escape trajectories is here carried out with an indirect method, which is based on the theory of optimal control and transforms the propellant minimization problem into a multipoint boundary value problem (BVP). The BVP is solved with an iterative single-shooting procedure based on Newton's method. High-accuracy results were sought. The dynamic model considers four-body gravitation (spacecraft, subject to Earth, Moon, and Sun gravity), JPL ephemeris for the position of the bodies, and solar radiation pressure (SRP). It also includes an 8×8 spherical harmonic model for Earth [15,16], even though its effect is negligible as no close passage occurs; the harmonic model for the Moon is here neglected but can be easily implemented if needed.

Indirect methods are computationally efficient but may suffer from poor convergence. Techniques to address numerical issues and to find proper tentative solutions are here introduced. The present analysis considers escapes from L2 and does not impose a constraint on the escape velocity direction. Analysis and results are to be transitioned in future studies on escape trajectories for specific missions. A proper tentative solution is needed, and the use of partial solutions and/or solutions of simpler problems is often an effective means to find such tentative solutions [17]. The solutions obtained here are suitable as tentative guesses for escape from orbits with practical uses, such as NRHOs, and linked to the analysis of the interplanetary phase for the joint optimization of escape and interplanetary transfer to the selected interplanetary destination [18].

In the recent literature, Ref. [19] considered evasion from SEL2 in the circular restricted three-body problem. Direct escape was compared to trajectories with Earth gravity assist; impulsive maneuvers were first considered and then extended to EP, using direct collocation and a nonlinear programming optimization scheme. The analysis is here extended to take orbit eccentricity and Moon gravity into account. In the Earth-Moon system, access to LPs was analyzed in Ref. [20], but the emphasis was not on EP escape trajectories. Impulsive escape trajectories from EML2 were analyzed in Ref. [21] in the Sun-Earth-Moon bi-circular restricted four-body problem, either for direct escape or via Earth swing-by; the Sun gravitational perturbation and the relative Moon angular position were both considered. Here the analysis is extended by implementing the use of EP, the JPL's DE430 ephemeris, and a higher fidelity model for non-assisted EML2 escapes. Results will highlight the influence that the most relevant parameters (e.g., time of flight, positions of the perturbing bodies with respect to each other and to the spacecraft) have on propulsive requirements and characteristics of the optimal escape trajectories.

Section 2 introduces the dynamic model with a detailed analysis of the relevant perturbations taken into consideration. Section 3 describes how the optimal control problem is developed and implemented. Sections 4 and 5 show the optimal trajectories obtained for departures, respectively, from SEL2 and EML2; both sections include subsections resulting from trajectories obtained with different boundary conditions. Section 6 provides examples of applications of the results. Finally, Section 7 presents the paper's conclusions.

2. Dynamic Model

The dynamic model considers a point-mass spacecraft with variable mass. The problem state variables are position r , velocity V , and mass, m , of the spacecraft, and are ruled by the following differential equations:

$$dr/dt = V \tag{1}$$

$$dV/dt = -\mu r/r^3 + T/m + a_J + a_{lsg} + a_{srp} \tag{2}$$

$$dm/dt = -T/c \tag{3}$$

where $-\mu r/r^3$ is the spherical Earth gravitational acceleration, a_J is the perturbing acceleration due to Earth’s non-sphericity, a_{lsg} is the perturbing acceleration due to Moon (lunar) and Sun (solar) gravity (i.e., lunisolar effect), and a_{srp} is the perturbation due to SRP. The trajectory is controlled by the thrust vector T . The available power and thrust are inversely proportional to the squared distance from the Sun, assuming efficiency, η_T , and effective exhaust velocity, c , as constants— $T = 2(\eta_T/c)P_1/R_s^2 = T_1/R_s^2$ —where P_1 and T_1 are the values at 1 AU and R_s is expressed in AU.

The Earth Mean Equator and Equinox of Epoch J2000 frame (i.e., EME2000) is adopted (Figure 1); I, J, K are unit vectors along the reference axes of EME2000. Precession and nutation are neglected. Right ascension ϑ and declination φ are introduced along with the radius magnitude r to write the position vector as $r = r \cos \vartheta \cos \varphi I + r \sin \vartheta \cos \varphi J + r \sin \varphi K$. The topocentric RF, identified by unit vectors i (radial), j (eastward), and k (northward) is introduced. The unit vectors are defined by the following:

$$\begin{Bmatrix} i \\ j \\ k \end{Bmatrix} = \begin{bmatrix} \cos \vartheta \cos \varphi & \sin \vartheta \cos \varphi & \sin \varphi \\ -\sin \vartheta & \cos \vartheta & 0 \\ -\cos \vartheta \sin \varphi & -\sin \vartheta \sin \varphi & \cos \varphi \end{bmatrix} \begin{Bmatrix} I \\ J \\ K \end{Bmatrix} \tag{4}$$

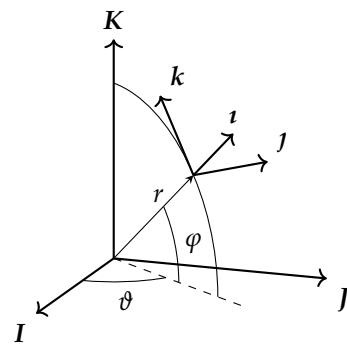


Figure 1. EME2000 vs. topocentric RF.

The position vector in the topocentric frame is $r = r i$ and the velocity vector is expressed as $V = \dot{r} = u i + v j + w k$, with u, v , and w as the radial, eastward, and northward components, respectively. The seven scalar state equations are easily derived as

$$dr/dt = u \tag{5}$$

$$d\vartheta/dt = v/(r \cos \varphi) \tag{6}$$

$$d\varphi/dt = w/r \tag{7}$$

$$du/dt = -\mu/r^2 + (v^2 + w^2)/r + T_u/m + (a_J)_u + (a_{lsp})_u + (a_{srp})_u \tag{8}$$

$$dv/dt = (-uv + vw \tan \varphi)/r + T_v/m + (a_J)_v + (a_{lsp})_v + (a_{srp})_v \tag{9}$$

$$dw/dt = (-uw - v^2 \tan \varphi)/r + T_w/m + (a_J)_w + (a_{lsp})_w + (a_{srp})_w \tag{10}$$

$$dm/dt = -T/c \tag{11}$$

Boundary conditions contain initial values of position $(r_0, \theta_0, \varphi_0)$, velocity (u_0, v_0, w_0) , and mass (m_0) , and final values of r_f . Constraints on either the final value of $C_3 = u_f^2 + v_f^2 + w_f^2 - 2\mu/r_f$ or the final time may be introduced. No constraint is imposed on the final value of the terrestrial longitude and latitude. The final mass is maximized. The perturbation due to Earth’s harmonic potential was already present in the dynamical model and has been maintained, even though it has negligible influence on results and speed of calculations—it is described in Refs. [15,16]; details are here omitted for the sake of conciseness. Results show that SRP has a negligible influence on performance for the present study, causing variations of the final mass of a few grams. Nevertheless, the SRP perturbation is included in the integration (for further references, please refer to Ref. [15]), but it is not further analyzed in the results.

Lunisolar Effect

DE430 JPL ephemerides [22] are used to retrieve Moon (subscript ℓ) and Sun (subscript s) positions. If subscript b is used to indicate a generic body, its position vector r_b is given in rectangular coordinates x_b, y_b, z_b with respect to the Earth in the international celestial reference frame (ICRF), i.e., $r_b = x_b\mathbf{I} + y_b\mathbf{J} + z_b\mathbf{K}$. The small differences between ICRF and EME2000 are neglected, and the latter is used in the present analysis. The gravitational perturbation caused by the body, which has gravitational parameter μ_b and position vector with respect to the Earth r_b , is obtained as the difference of the gravitational accelerations on spacecraft (a_{bg}) and Earth (a_{bE}). One has

$$a_{bg} = -(\mu_b/R_b^3)\mathbf{R}_b - (\mu_b/r_b^3)r_b \tag{12}$$

where $\mathbf{R}_b = r - r_b$ is the spacecraft relative position vector (and $-r_b$ is Earth’s relative position) with respect to the perturbing body. A schematic representation is provided in Figure 2 below.

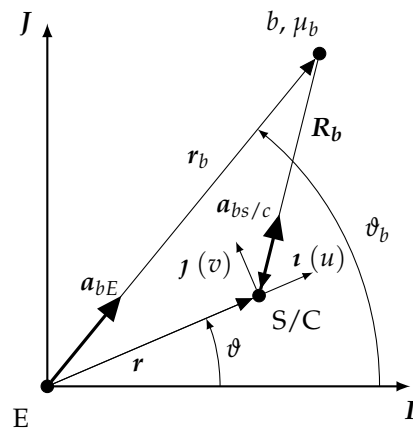


Figure 2. Schematic representation of gravitational perturbation in EME2000 RF.

The acceleration is projected onto the topocentric frame at epoch to easily obtain the perturbing components. When the perturbing body is very far compared with the Earth–spacecraft distance (i.e., when $r_b \gg r$, as it happens for the Sun) and coplanarity is assumed, a simple expression of the tangential and radial components of the perturbation can be derived (please refer to Refs. [15,16] for further details).

$$(a_{ss/c} - a_{sE}) \cdot \hat{u}_j = \frac{3}{2} \frac{\mu_s}{r_s^3} \sin [2(\theta_s - \theta)] \tag{13}$$

$$(a_{ss/c} - a_{sE}) \cdot \hat{u}_i = \frac{3}{2} \frac{\mu_s}{r_s^3} \{1 + \cos [2(\theta_s - \theta)]\} \tag{14}$$

where \hat{u}_j and \hat{u}_i are, respectively, the tangential and radial unit vectors.

The spacecraft velocity has main components along tangential and radial directions, so these terms can be used to estimate the positive or negative effects of solar perturbation during the escape. Equations (13) and (14) show that it is possible to enclose the perturbation effect dependence on Sun–spacecraft position in the two following proportionality terms:

$$\zeta_v = \sin(2\Delta\theta) \quad (15)$$

$$\zeta_u = 1 + \cos(2\Delta\theta) \quad (16)$$

where $\Delta\theta$ is the angular difference between the Sun and the spacecraft. Energy is increased by the acceleration component along the spacecraft direction. Large positive ζ_v tends to be more useful during the initial phase (tangential velocity), whereas large ζ_u should be preferred in the final phases, when the velocity tends to the radial direction. Large ζ_v occurs when the Sun is in the first ($0^\circ < \Delta\theta < 90^\circ$) or third ($-180^\circ < \Delta\theta < -90^\circ$) quadrant in the spacecraft rotating frame, whereas other $\Delta\theta$ combinations may have null or negative influence on the spacecraft energy if the spacecraft is continuously moving outward. The radial acceleration, on the other hand, cannot produce a negative effect (unless the spacecraft is moving towards the Earth) and has a maximum positive influence when the Sun is in between the fourth and first quadrants ($-45^\circ < \Delta\theta < 45^\circ$) or in between the second and the third quadrants ($\Delta\theta > 135^\circ$ and $\Delta\theta < -135^\circ$). In general, the combined effect of the two solar perturbation components may produce an overall positive effect on the spacecraft energy when the Sun is either close to -157.5° or $+22.5^\circ$ with respect to the Earth–spacecraft direction.

3. Optimization

The theory of optimal control [23,24] is applied to the differential system described above to determine the optimal solution for escape. The final mass is maximized, given the initial state (position, velocity, and mass) and the final distance from the Earth. The final time and/or the final value of C_3 may be added to the boundary conditions. Thrust (magnitude, constrained between 0 and the maximum available value, and direction) is the control variable. Adjoint variables λ are coupled to the state differential equations and the Hamiltonian is defined as $H = \lambda_r^T \mathbf{V} + \lambda_V^T (-\mu \mathbf{r}/r^3 + \mathbf{T}/m + \mathbf{a}_J + \mathbf{a}_\ell + \mathbf{a}_s) - \lambda_m T/c$. Euler–Lagrange equations provide differential equations for the adjoint variables; they are presented in Appendix A, and additional details can be found in Ref. [15]. The Hamiltonian must be maximized by the optimal controls, i.e., thrust magnitude and direction, in agreement with Pontryagin’s maximum principle (PMP). The thrust T must be parallel to the adjoint vector λ_V , also named the primer vector. The Hamiltonian is rewritten as $H = \lambda_r^T \mathbf{V} + \lambda_V^T (-\mu \mathbf{r}/r^3 + \mathbf{a}_J + \mathbf{a}_\ell + \mathbf{a}_s) + T(\lambda_V/m - \lambda_m/c)$, and is linear with respect to T ; a bang–bang control arises and the thrust must be maximized, $T = T_{max}$, when the switching function $S_F = \lambda_V/m - \lambda_m/c > 0$, while the thrust shall be null $T = 0$, when $S_F < 0$. Singular arcs, usually associated with atmospheric flight, are here excluded.

The handling of thrust discontinuities is one of the main challenges in indirect optimization, because they can create numerical problems in the gradients evaluation. Several techniques have been used to deal with this problem, such as smoothing techniques [25–27] or homotopy and continuation approaches [28,29]. More recently, new regularization techniques, such as uniform trigonometrization methods [30] and integrated control regularization methods [31], have also been introduced to handle thrust discontinuities and other kinds of path constraints.

In this analysis, a different approach is adopted. The switching structure (i.e., a suitable sequence of thrust and coast arcs) is specified a priori, and modified if PMP is violated. The simplest thrust–coast structure is initially assumed and eventually modified when required, according to PMP. Each trajectory is divided into a number of distinct phases equal to the number of thrust and coast arcs specified, thus producing a multipoint boundary value problem. The duration of each j -th phase, Δt_j , is unknown and subject to optimization. Additional boundary conditions specify that the switching function must be null at the

switching points, where the engine is turned on or off. This approach guarantees improved numerical accuracy and convergence speed/robustness compared with the alternative strategy of deciding the thrust level during integration, according to the instantaneous value of the switching function.

The equations are integrated by using a variable-order, variable-step integration scheme based on Adams–Moulton formulas. The achieved numerical accuracy is therefore comparable to the one obtained via high-precision orbital propagators in commercial or open-source software, such as STK or GMAT; as expected for indirect methods, computational times are minimal—below 10 seconds per trajectory on a standard 2.70 GHz CPU laptop—if the initial guesses are within a reasonable error range.

The initial values for some variables, e.g., the adjoint variables, are generally unknown. In order to solve the BVP, a Newton's scheme is adopted. Tentative values q are assumed for the unknowns (switching/final times and unknown adjoint initial values) and the error on the boundary conditions is determined after integration. Each i -th component of q is perturbed by a small quantity δq_i (e.g., 10^{-7}) and the variation of the error $\Delta\chi$ is evaluated, again after integration. The unknowns are corrected at each iteration, aiming at nullifying the errors by assuming linear behavior and evaluating numerically the error–gradient matrix $\partial\chi/\partial q = \Delta\chi/\partial q$, so that

$$\Delta q = -K[\partial\chi/\partial q]^{-1}\chi \quad (17)$$

where K is a relaxation parameter. Values between 0.01 and 1 are usually suited to obtain convergence.

A suitable tentative guess can be built from simple considerations. Given the initial state, a switching structure with a thrust arc followed by a coasting arc can initially be assumed. The length of the burn can be estimated from the available thrust acceleration, assuming a reasonable ΔV (e.g., 50–100 m/s for these cases). The velocity adjoint vector is taken parallel to the spacecraft velocity (energy gain is usually sought), with a magnitude that makes the switching function positive. The position adjoint vector is taken in the radial direction and with magnitude to have a decreasing magnitude of primer vector and switching function. Once a solution for a specific case is found, it can be used as a tentative guess for different scenarios (e.g., departure date, constraints on escape C_3 , etc.).

The boundary conditions at escape are geocentric. In addition to the final radius, the escape characteristic energy, and therefore C_3 , may also be specified. It follows that the same geocentric C_3 can produce different heliocentric energies based on the escape direction, which is here not constrained. The Results Section will present some observations about the heliocentric escape conditions, but a detailed analysis is left for future studies.

4. Escape Trajectories from Sun-Earth L2

In 2018, the European Space Agency proposed an F-class mission [32] departing from SEL2, where the spacecraft is carried as a piggyback of the ARIEL or PLATO missions. The spacecraft would remain in L2 for a suitable time and then depart from this point for an interplanetary trajectory; the escape trajectory is analyzed here. According to the preliminary mission specifications, a spacecraft mass of 850 kg is considered. The propulsion system is based on the performance of the ArianeGroup RIT 2X: Power available to the thruster $4.2/R_s^2$ kW (distance from the Sun R_s in AU), constant efficiency 0.625, constant specific impulse 3300 s, with the thrust that scales as power.

Departures from the Lagrangian point L2 of the Sun-Earth system are considered. The initial distance from the Earth is the radius of Hill's sphere, evaluated by supposing that the mass of the smaller primary (Moon with respect to Earth or Earth with respect to Sun) is much smaller than the bigger primary. Velocity is selected to have the same angular velocity of the primaries relative motion. One has

$$r_0 = r_{s,0}[1/(3\mu_s)]^{1/3} \quad (18)$$

$$\vartheta_0 = \vartheta_{s,0} + \pi \quad (19)$$

$$\varphi_0 = -\varphi_{s,0} \quad (20)$$

$$u_0 = 0 \quad (21)$$

$$v_0 = v_{s,0}(r_0/r_{s,0}) \quad (22)$$

$$w_0 = -w_{s,0}(r_0/r_{s,0}) \quad (23)$$

where $r_{s,0}$ is the Sun-Earth distance at epoch t_0 . Quantities are here normalized by using Earth's ellipsoid major semi-axis $r_E = 6378.1363$ km and the corresponding circular velocity $\sqrt{\mu_E/r_E}$ as reference values, where $\mu_E = 398,600.4415$ km³/s² is Earth's gravitational parameter. The normalized gravitational parameter of the Earth is equal to one.

The reference departure date is 15 October 2025, when the instantaneous Earth-Moon distance matches its average value of 384,400 km. The analysis time is extended up to the point in which the instantaneous Earth-Moon distance is again at the average value, which happens on 12 November 2025. Five sample cases are of interest, namely one each week, hereinafter referred to as cases 1–5.

SEL2 departures have been analyzed under different constraints. In particular, the distance of escape is always fixed at 3 million km from the Earth, namely beyond Earth's sphere of influence (SOI), when the combination of gravitational attractions of Earth and Moon becomes negligible compared with the Sun's one. The first analysis bounds the time to escape at 90 days, while leaving the final energy as a free parameter. Then, escape C_3 equal to 0.2 and 0.5 (km/s)², with no constraints on the escape time will be considered.

4.1. Sun-Earth L2 Escapes with Constrained Final Time

The solutions for the five departure dates show a common trend during the escape. Figure 3 highlights a whole family of solutions (represented by the hundreds of subtle lines) with departures starting from case 1, on 15 October 2025, up to case 5, on 12 November 2025. These selected five cases are henceforth highlighted with specific styles. A family collects solutions that can be found with a continuation approach: There are close similarities, and, at a first approximation, each curve seems simply rotated due to the different departure position. Each trajectory is however different, mainly due to the Moon position during flight, which changes with the departure date.

The spacecraft is actually pulled towards the boundary of the SOI by the Sun, which has a large positive overall effect on the orbit energy. Its direction at the beginning and at the end of each selected escape is represented in the lower part of the figure. Thrust is therefore used to achieve a trajectory that maintains the Sun in a favorable position, maximizing the effect of its pull ($\Delta\vartheta$ close to 180°, see Figure 4). Figure 5 shows that for the selected SEL2 escapes the whole energy gain, except for a minor thrust contribution at the beginning, is due to the solar perturbation. Please note that, henceforth, thrust phases are shown as bold lines in those figures that may contain that information.

Thrust is used so that the Sun moves from the second to the third quadrant of the frame that rotates with the spacecraft, where Sun's gravity acts to increase the orbit energy. The spacecraft remains close to 180° and/or between −135° and −180° in the rotating frame, exploiting both tangential and radial components of Sun's perturbation. The same trend is shown for different departure dates, with the initial thrust arc adapting to produce the same effects, as shown in Figure 4. In a Sun-Earth synodic RF centered on Earth (Figure 6), such trajectories are all located in the fourth quadrant and show evident similarities during the escape.

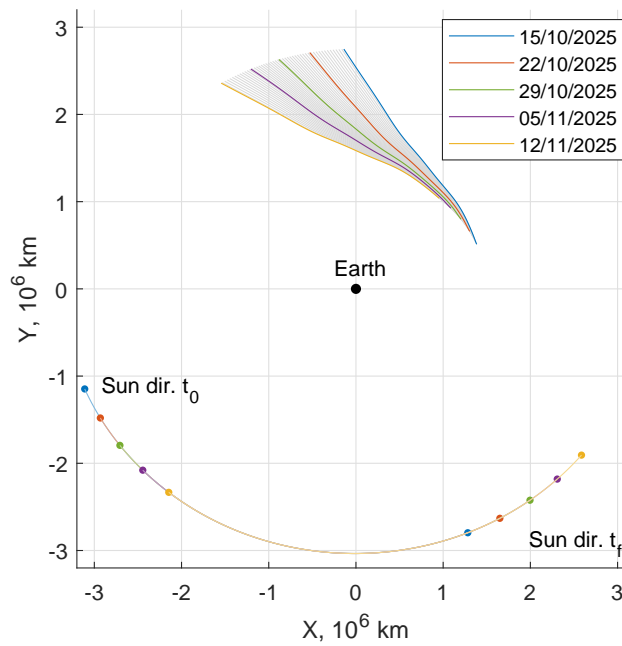


Figure 3. SEL2 escape trajectories over a lunar month, fixed $t_f = 90$ days, free C_3 , EME2000 RF.

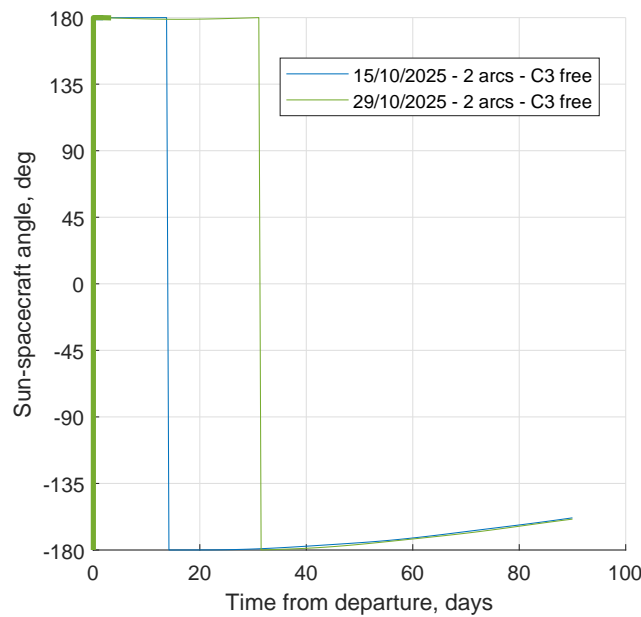


Figure 4. Time evolution of Sun–spacecraft relative angle for two SEL2 case studies.

The effects of Moon’s perturbation are shown in Figure 7, which presents the trend of the propellant requests, and thus the ΔV , to reach an escape in 90 days with free final energy. The reference departure date (15 October 2025) is in the region where ΔV and C_3 values are lowest. The spacecraft is relatively far from the Moon, and Moon’s gravity acts mainly on the Earth. The initial geometry on the reference departure date shows that the Moon reduces the spacecraft’s geocentric energy by pulling the Earth; this perturbation modifies the Sun–Earth–spacecraft geometry so that the Sun’s pull on the spacecraft is increased, and a lower propulsive effort is needed. The opposite happens after half the lunar period. The final value of C_3 depends on the energy gain provided by thrusting and the overall effect of the perturbing bodies, causing oscillations in the trajectory performance.

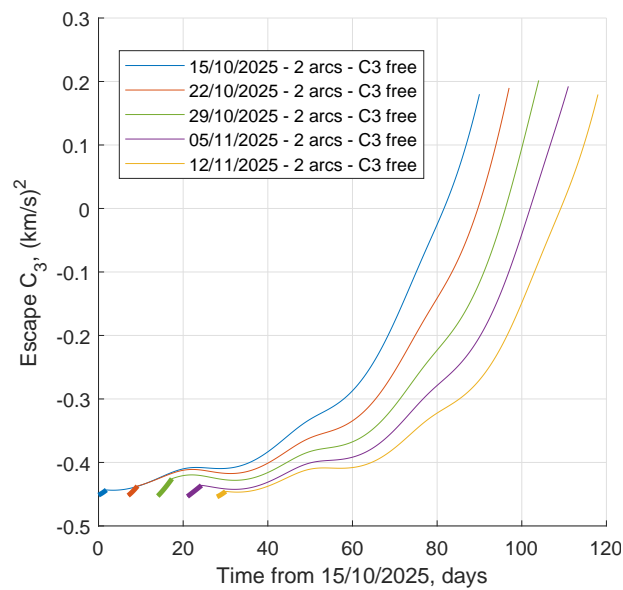


Figure 5. Spacecraft energy over time for reference departure dates from SEL2.

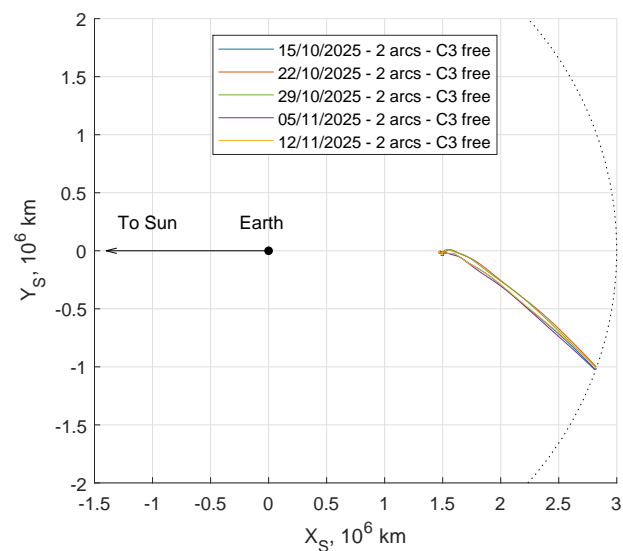


Figure 6. SEL2 case study escape trajectories in the Sun-Earth rotating RF.

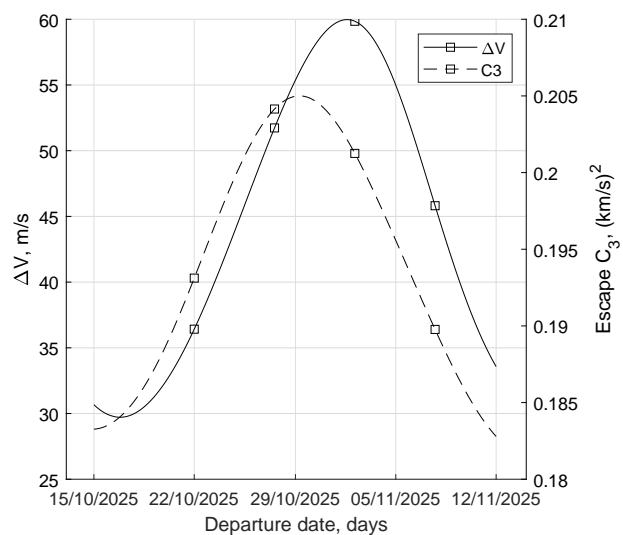


Figure 7. Influence of departure date to escape from SEL2—fixed $t_f = 90$ days, free C_3 .

The effect of Sun’s pull is dominant, and two simple coefficients are defined to assess how much the influence of the solar perturbation is acting favorably on the escape, $\eta_{SP,u}$ and $\eta_{SP,v}$. The radial and tangential perturbation weights are introduced to evaluate the normalized contributions of solar perturbation along the whole trajectory. The trajectory is split into n uniform intervals and $\eta_{SP,u}$ and $\eta_{SP,v}$ are evaluated as

$$\eta_{SP,u} = \frac{1}{2\Delta t_{max}} \left(\sum_{j=1}^{n-1} \frac{\xi_{u,j} + \xi_{u,j+1}}{2} \Delta t_j \right) \tag{24}$$

$$\eta_{SP,v} = \frac{1}{\Delta t_{max}} \left(\sum_{j=1}^{n-1} \frac{\xi_{v,j} + \xi_{v,j+1}}{2} \Delta t_j \right) \tag{25}$$

For each family of solutions, the η_{SP} are normalized with respect to the longest mission among them. This allowed us to produce a general parameter able to compare those escapes with a different total duration.

The 1/2 coefficient in $\eta_{SP,u}$ is introduced to make $\eta_{SP,u} = 1$ for maximum favorable effect, whereas $\eta_{SP,u} = 0$ corresponds to null effect. The values of $\eta_{SP,v}$, instead, range between -1 (most unfavorable) and 1 (most favorable). Figure 8 shows the trend of these coefficients; it is clear that SEL2 escapes exploit mostly the radial perturbation, with slight fluctuations of the tangential perturbation that, however, acts always favorably. Even though they are not an exact measure of solar effect, these coefficients correctly match the actual propellant consumption trend, with minimum propellant requirements in the region between maximum $\eta_{SP,u}$ and $\eta_{SP,v}$.

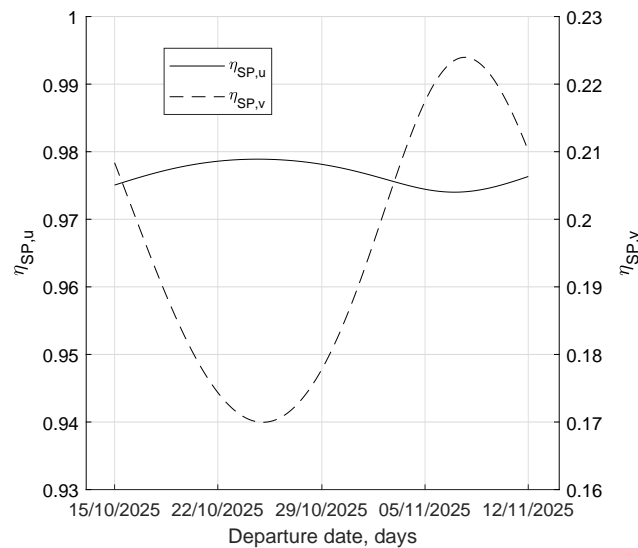


Figure 8. Radial and tangential overall perturbation effect per trajectory for escapes from SEL2.

Table 1 compares the performance of the reference cases $C = 1-5$, depending on the departure date. All the solutions belong to the same family ($f = I$) and have a 2-phase structure ($p = 2$).

Table 1. SEL2 escapes performance—fixed $t_f = 90$ days, free C_3 .

C	f	p	$\eta_{SP,u}$	$\eta_{SP,v}$	$\overline{\eta_{SP}}$	ΔV m/s	$C_{3,f}$ (km/s) ²
1	I	2	0.975	0.208	0.592	30.676	0.1833
2	I	2	0.979	0.174	0.576	36.419	0.1931
3	I	2	0.978	0.178	0.578	55.369	0.2050
4	I	2	0.974	0.217	0.596	54.982	0.1956
5	I	2	0.976	0.210	0.593	33.572	0.1828

4.2. Sun-Earth L2 Escapes with Constrained Final Energy

When the escape maneuver is the start of an interplanetary transfer, specific values of escape energy and C_3 could be sought. If the final C_3 value is constrained, then the escape trajectory is modified to change the overall effect of Sun's pull. Two case studies have been analyzed, by imposing the final C_3 equal to 0.2 and 0.5 (km/s)².

Given the high sensitivity of the convergence process to the adjoint variables initial values, both the exploration procedure to generate a family of solutions, and the passage from a solution with the same departure date to a new case with different final conditions, are particularly delicate. Compared with the previous study [16], various methodologies and techniques have been developed and implemented to guarantee robustness to the method and to automate many of these processes. The case studies solutions at fixed C_3 have been found one-by-one starting from a set of tentative solutions built on user experience (initial thrust aligned with velocity, thrust-coast structure). The other solutions have been found similarly or via an ad hoc continuation method. A gradual variation is imposed, starting from the free final C_3 solution towards the constrained one (or from the lower to the higher constrained final C_3) or using the closest available solution in terms of departure date as a tentative guess. It can happen that a forward search from a certain date and a backward search from a later date do not end up to the same point; therefore, for the same departure date, solutions belonging to different "families" are found.

This bifurcation phenomenon is visible in Figure 9 (left), which shows that three families of solutions arise from the single family at fixed escape time when solutions are forced to $C_3 = 0.2$ (km/s)². On the contrary, all the solutions for $C_3 = 0.5$ (km/s)² have the same strategy. Analogous considerations are shown in Figure 10, in which all the trajectories reach the same final C_3 but with different costs and mission durations.

The first family is found for departure between 15 October 2025 and 21 October 2025, with trajectories that tend to be radial and have short trip times. The second family is for departures between 18 October 2025 and 2 November 2025. The third family extends over the whole launch period considered, and has trajectories with a more tangential velocity with respect to the other solutions. This result shows how, for the same departure date, it is possible to pick different strategies according to the specific needs; at the same time, it is clear that the improved code allows the indirect method to find various solutions without falling in the same local minima. In this case, family III is always the better solution for what concerns propellant consumption, but different constraints (C_3 value, additional time constraints) may change the scenario.

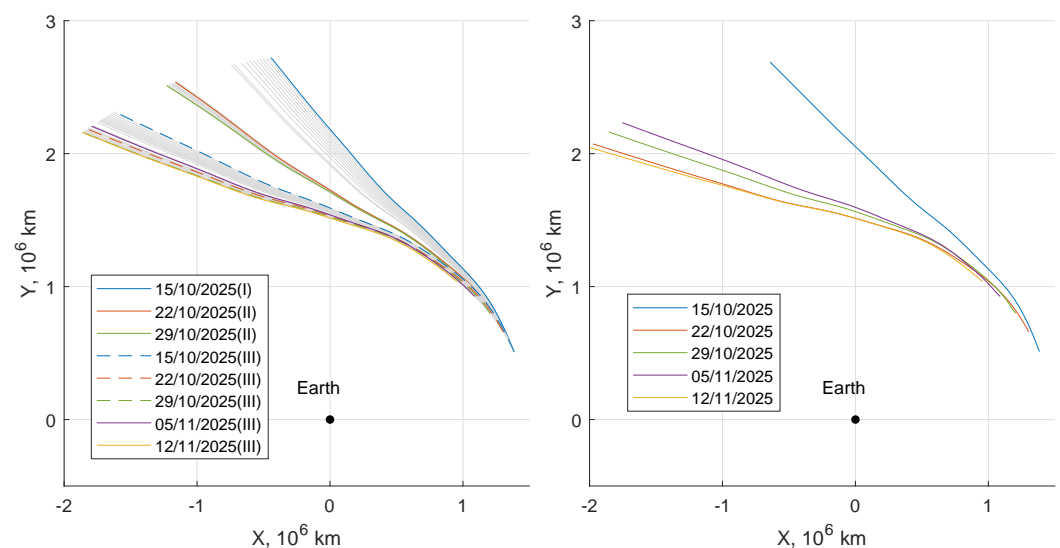


Figure 9. SEL2 escape trajectories over a lunar month—fixed $C_3 = 0.2$ (km/s)² (left), 0.5 (km/s)² (right), free t_f , EME2000 RF.

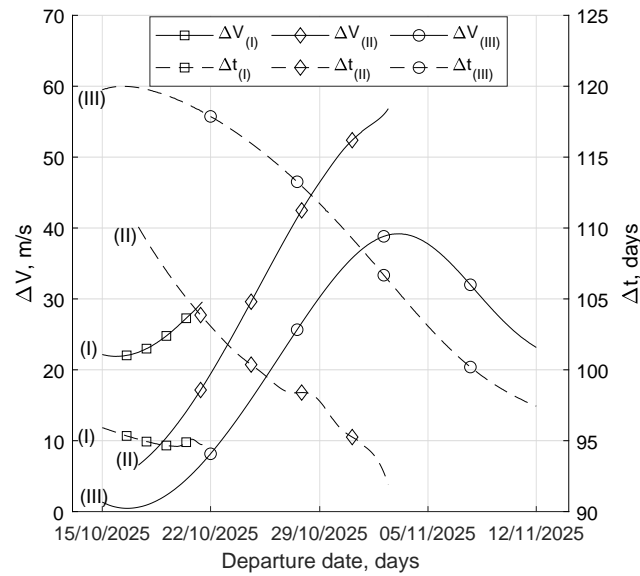


Figure 10. Influence of departure date to escape from SEL2—families of solutions—fixed $C_3 = 0.2 \text{ (km/s)}^2$, free t_f .

Figure 11 shows the trend of the spacecraft energy over time. It can be seen that the solution with final $C_3 = 0.5 \text{ (km/s)}^2$ includes an evident second thrust arc (T) after a coast arc (C), for a total of three phases in a T–C–T strategy. In this case, later thrusting is preferred to achieve the desired large final energy, instead of increasing the initial burn duration, in order to maintain an unaltered positive effect of solar perturbation.

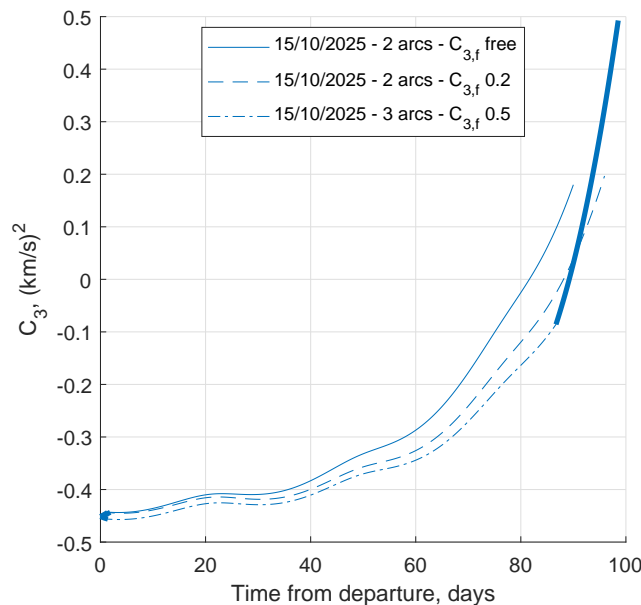


Figure 11. Spacecraft energy over time from SEL2—comparison between free and fixed final C_3 .

Tables 2 and 3, instead, show the solutions for the escapes with fixed final energy, while in the lower final energy scenario multiple families of solutions arise, in which some trajectories exploit more consistently the solar perturbation, whereas others use more propellant, the scenario with higher final energy only relies on a second consistent final burn to reach the desired final energy as the only feasible option. Figure 12 shows the semi-major axes of all these trajectories in the heliocentric ecliptic reference frame, on the left for the lower energy scenario and on the right for the higher one. The integration is extended to 2.5 times the time to escape to show the evolution after the exit from Earth’s SOI; while

for the final $C_3 = 0.2 \text{ (km/s)}^2$ case, this operation produces a simple extension of the final coasting phase, in the $C_3 = 0.5 \text{ (km/s)}^2$ scenario, the appearing of a fictitious terminal fourth coasting phase is needed. All the trajectories have similar trends with comparable costs, almost equal use of the solar perturbation and similar final energies. However, as anticipated, the escape directions are different; therefore, the orbital parameters, as shown in Figure 12, show slightly different trends. It is worth noting that small variations occur after the escape for the residual influence of Earth’s gravity. Nevertheless, departures spaced apart by one lunar month overlap again quite precisely.

Table 2. SEL2 escapes performance—fixed $C_3 = 0.2 \text{ (km/s)}^2$, free t_f .

C	f	p	$\eta_{SP,u}$	$\eta_{SP,v}$	$\overline{\eta_{SP}}$	ΔV m/s	t_f days
1	I	2	0.782	0.160	0.471	22.155	95.92
2	II	2	0.842	0.162	0.502	19.416	103.08
3	II	2	0.795	0.181	0.488	46.462	97.78
1	III	2	0.980	0.193	0.586	1.346	119.75
2	III	2	0.965	0.164	0.564	8.153	117.87
3	III	2	0.914	0.158	0.536	30.253	111.72
4	III	2	0.841	0.173	0.507	37.757	103.07
5	III	2	0.796	0.162	0.479	23.155	97.44

Table 3. SEL2 escapes performance—fixed $C_3 = 0.5 \text{ (km/s)}^2$, free t_f .

C	f	p	$\eta_{SP,u}$	$\eta_{SP,v}$	$\overline{\eta_{SP}}$	ΔV m/s	t_f days
1	I	3	0.805	0.199	0.502	220.205	98.60
2	I	3	0.983	0.173	0.578	222.191	119.15
3	I	3	0.898	0.237	0.568	242.771	109.95
4	I	3	0.822	0.253	0.537	246.049	101.40
5	I	3	0.817	0.205	0.511	221.774	99.83

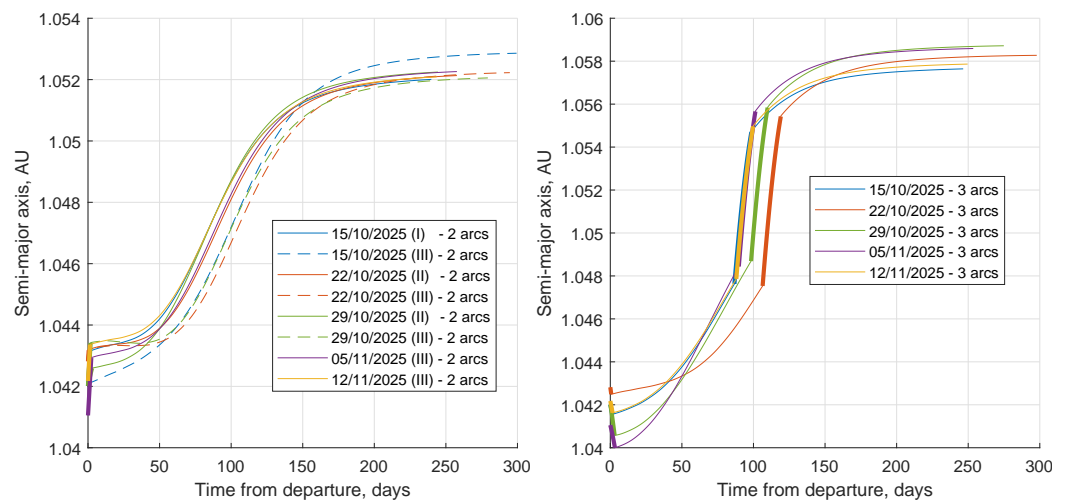


Figure 12. SEL2 selected escapes—spacecraft semi-major axis in the heliocentric ecliptic RF—fixed $C_3 = 0.2 \text{ (km/s)}^2$ (left), 0.5 (km/s)^2 (right) – $2.5 \times t_f$ propagation.

5. Escape Trajectories from Earth-Moon L2

The dynamics in the vicinity of EML2 is characterized by a complex gravitational interaction between the Sun, the Earth, and the Moon. Nevertheless, several researches and missions have exploited this region for the numerous strategic and design advantages that it can offer. Indeed, in 2004, the ESA’s Advanced Concepts Team researched the use of

Lagrange points as departure and arrival points of space missions, demonstrating that the characteristic orbits nearby of these points are accessible in reasonable times and costs [20].

Lissajous orbits around EML2 have been used for the Artemis P1 mission in 2010 and Chang'e 5-T1 in 2014. The recent Chang'e 4 mission used a halo orbit around EML2 for its relay satellite, Queqiao, which is positioned at EML2 since 2018 for signal-and-sunlight eclipses avoidance. The NASA's Exploration Campaign in 2018 assessed that the Artemis program would include the positioning of an outpost in the vicinity of EML2, the LOP-G, in a Southern Synodic 9:2 NRHO, that will serve to enable future deep space exploration missions. By the middle of 2022, the NASA Artemis 1 mission, formerly Exploration Mission 1, is expected to take place. NASA selected 13 secondary payloads to be transported in the new SLS Block 1, among which there will be EQUULEUS, a 6U Cubesat proposed by JAXA and the University of Tokyo [33]. Its primary goal is a low-energy trajectory control experiment near EML2; its mission and scientific objectives are discussed in Ref. [34].

These important missions and programs simultaneously show the high scientific interest and the complexities in the use of such L2 points. The proposed analysis implements direct escapes from EML2 and disregards the complexities that would derive from the inclusion of NRHOs or Lissajous orbits as departure points, which will be subject of future research. As per the SEL2 case, the propulsion system has the same values for power and efficiency, but the specific impulse is imposed constant at 2000 s, like in a typical, current Hall thruster.

The same specific five departure times in a lunar synodic period of the previous section are again considered to explore the effect of the relative position of the Moon and the Sun on the escape maneuver. The first (15 October 2025) and last (12 November 2025) departures happen at times with the nominal Moon's mean orbital radius; a perturbed Moon orbit is considered so the positions in EME2000 are slightly different. The linearized L2 distance is again used to define the spacecraft initial position. One has

$$r_0 = r_{l,0} \left[1 + (\mu_\ell/3)^{1/3} \right] \quad (26)$$

$$\vartheta_0 = \vartheta_{l,0} \quad (27)$$

$$\varphi_0 = \varphi_{l,0} \quad (28)$$

$$u_0 = u_{l,0} \quad (29)$$

$$v_0 = v_{l,0}(r_0/r_{l,0}) \quad (30)$$

$$w_0 = w_{l,0}(r_0/r_{l,0}) \quad (31)$$

The final radius is fixed at 3 million km, beyond Earth's SOI boundary. Like in the SEL2 departure analysis, three scenarios are considered: the first with a fixed time to escape and a free final energy, and other two with escape C_3 fixed at a lower (0.2 (km/s)^2) and higher (0.5 (km/s)^2) value with free time to escape.

5.1. Earth-Moon L2 Escapes with Constrained Final Time

In similarity to the escape from SEL2, single burn trajectories are initially sought; these trajectories are characterized by a first thrust (T) arc followed by a coast (C) arc.

Figure 13 shows the manifold of departure trajectories for the selected dates. Those trajectories exploiting a second burn are distinguished by a small dot at the arc end. The first (15 October 2025) and last (12 November 2025) departures, i.e., cases 1 and 5, have slightly different initial positions in EME2000 and the Sun relative angle has a difference of about 30° . Nonetheless, the two solutions are similar with a difference in spacecraft final angular positions close to the 30° between Sun positions. When additional departure dates are considered, three families of solutions can be distinguished (see also Figure 14). Due to the greater dynamic complexity of the Earth-Moon system, even the trajectories with fixed final time and free final energy split into several families. Table 4 shows the

performance for the selected departure dates in each family, and Figure 15 shows some of them to highlight the differences.

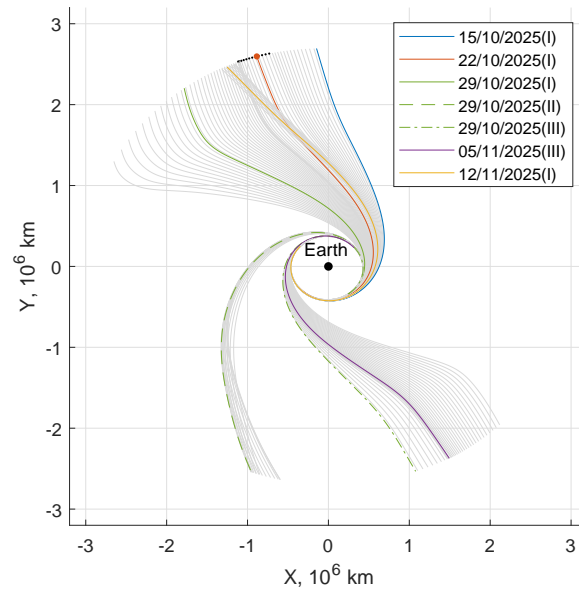


Figure 13. EML2 escape trajectories—fixed $t_f = 75$ days, free C_3 , EME2000 RF.

Table 4. EML2 escapes performance—fixed $t_f = 75$ days, free C_3 .

C	f	p	$\eta_{SP,u}$	$\eta_{SP,v}$	$\overline{\eta_{SP}}$	ΔV m/s	$C_{3,f}$ (km/s) ²
1	I	2	0.833	0.064	0.448	48.763	0.3510
2	I	4	0.783	−0.429	0.177	61.183	0.1523
3	I	2	0.503	−0.712	−0.105	161.279	0.0026
3	II	2	0.434	0.750	0.592	20.476	0.4789
3	III	2	0.805	−0.106	0.349	17.412	0.3108
4	III	2	0.801	−0.376	0.212	38.572	0.1821
5	I	2	0.775	0.302	0.538	51.373	0.4430

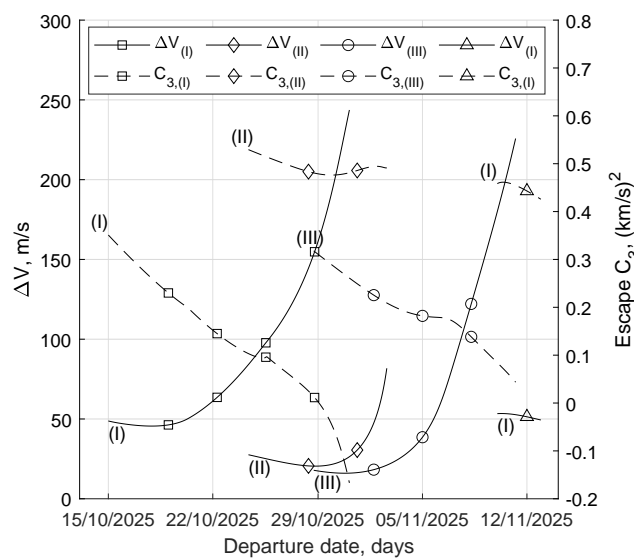


Figure 14. Influence of departure date to escape from EML2—families of solutions—fixed $t_f = 75$ days, free C_3 .

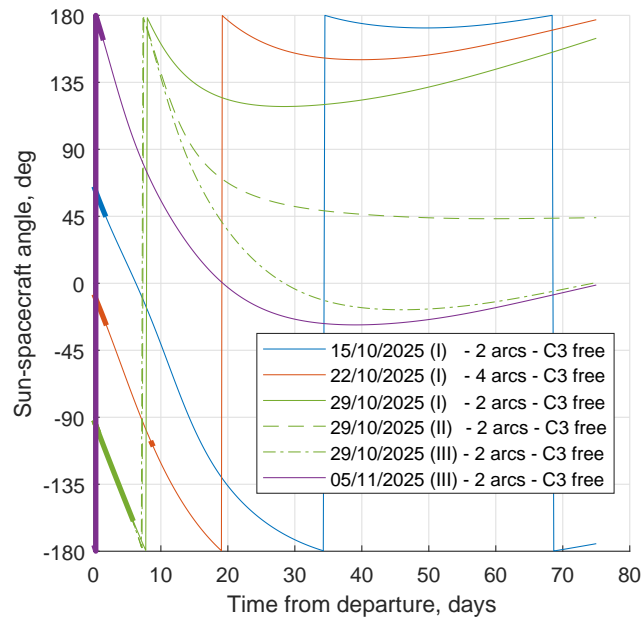


Figure 15. Time evolution of Sun–spacecraft relative angle for selected EML2 solutions.

In particular, by observing the same trajectories in the Sun–Earth synodic reference frame centered on Earth (Figure 16), three escape trends arise. Cases 1, 2, and 3 of family I occupy the first and fourth quadrants, favorably exploiting the radial component of Sun’s perturbation in the final part of the escape, in accordance with Figure 15. The spacecraft always shows terminal $\Delta\theta$ close to 180° , while case 2 exploits a short second burn to align the final leg of the trajectory, the late departure of case 3 forces a longer initial burn to achieve a similar result (Figure 16, right). The specular scenario, for cases 3 and 4 of family III, sees escape points on the L1 side (i.e., between Earth and Sun, see Figure 4). These trajectories occupy the second and third quadrants in the rotating reference frame, tending to null $\Delta\theta$, which, again, implies favorable radial perturbation. The single trajectory in the second quadrant, case 3 family II, exploits more substantially the tangential component with an escape tending to $\Delta\theta = 45^\circ$. The last trajectory, case 5, repeats the trend of family I solutions, being in particular very close, as expected, to the solution departing a lunar synodic month earlier, even though the different position of the Sun affects the trajectory details.

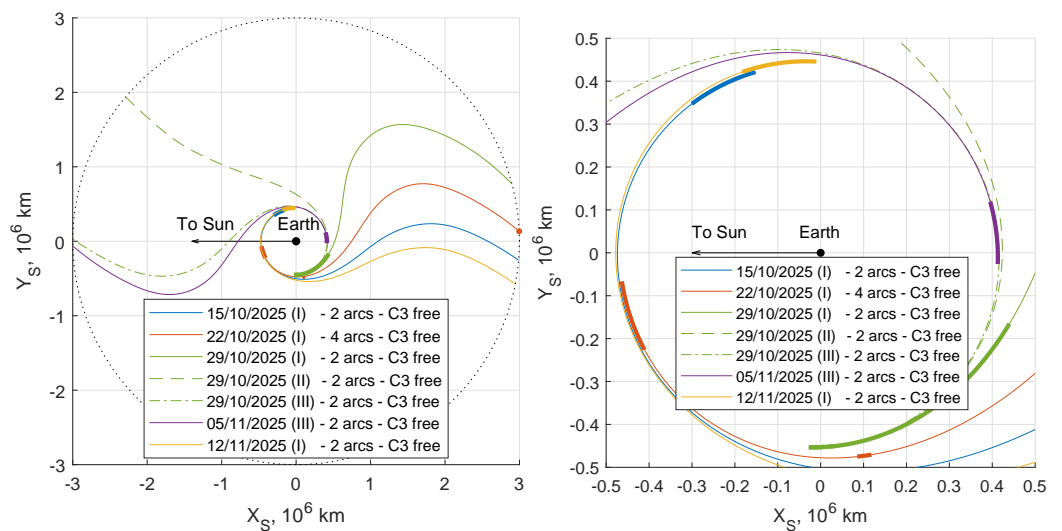


Figure 16. EML2 selected escape trajectories (left), departure detailed view (right), Sun–Earth synodic RF.

The reference departure date has a T–C escape strategy with low propellant consumption, which corresponds to a positive use of both the tangential and radial solar perturbation as seen from the evolution of the relative angle between the spacecraft and the Sun. The same switching structure does not respect PMP for the second departure date. In this case, the switching function becomes negative during the thrust arc, suggesting that the thruster should be turned off. The switching structure is modified in agreement with this behavior and a four-arc trajectory, T–C–T–C, is adopted. The two-burn solution respects PMP and is therefore optimal; the propellant consumption is correspondingly reduced with a significant improvement. Case study 3 has solutions pertaining to three different families, and by analyzing the Sun–spacecraft relative angle from family I to family III, one can notice that increasingly improved strategies can be implemented. The first family shows a very high propellant usage to contrast the long period (roughly, between 15 and 50 days since departure) in which the spacecraft is at a null or negative configuration for the tangential perturbation. The second family has a similar condition but has favorable radial perturbations, leading to a wider trajectory at a lower cost. The third family, which spans also to the fourth departure date, is the most favorable one, and it exploits a consistently positive tangential perturbation. Indeed, even if cases 3 and 4 from family III have departures separated by 90° , they tend to both end at $\Delta\theta \approx 0^\circ$. The same considerations are highlighted in Figure 17.

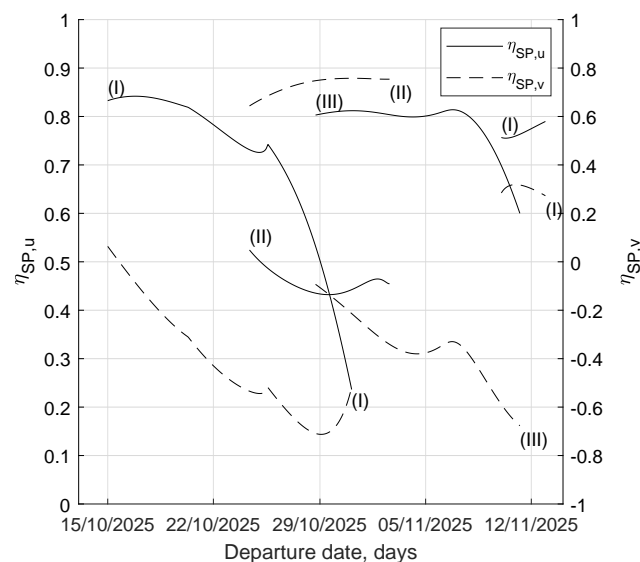


Figure 17. Radial and tangential overall perturbation effect per trajectory for escapes from EML2.

It is noteworthy that the second family of solutions has a very low propellant consumption with a very high free final energy, implying that constrained final energy solutions, especially the ones fixed at lower values, will have to reduce somehow the spacecraft energy to achieve the desired boundary conditions. The same applies to part of family III solution and to case 5 (family I).

5.2. Earth-Moon L2 Escapes with Constrained Final Energy

The trajectories with fixed final energy have been calculated with the same strategies implemented for the SEL2 case. The complexities due to the proximity of the Moon and the perturbations of the third body divide more evidently the families of solutions compared to the cases with free final energy. Figure 18 shows on the left all the solutions found for the fixed low energy scenario, while on the right those for $C_3 = 0.5 \text{ (km/s)}^2$. The families still have many solutions within them, but most of them tend to overlap in their final phase when the final energy is fixed.

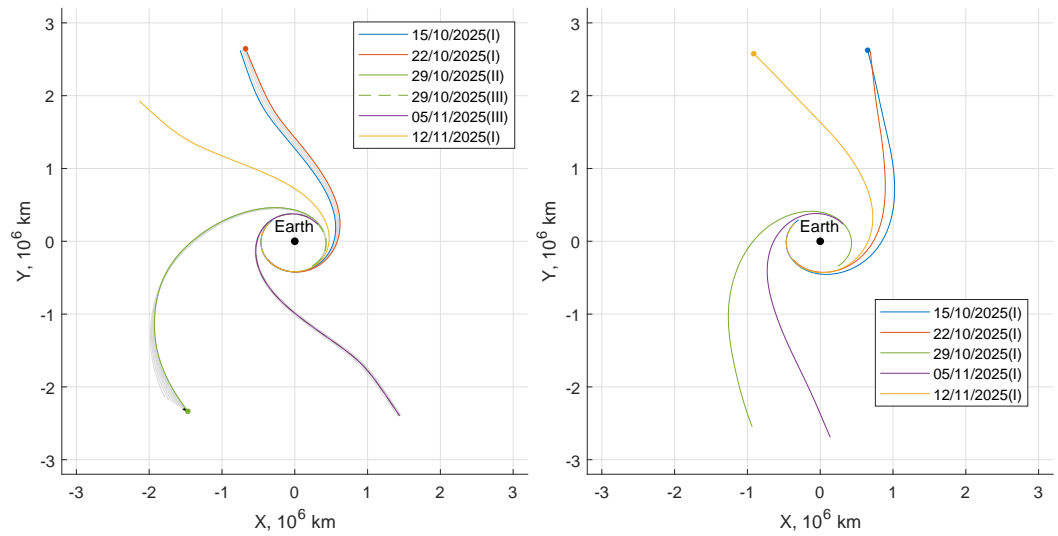


Figure 18. EML2 escape trajectories over a lunar month—fixed $C_3 = 0.2 \text{ (km/s)}^2$ (left), 0.5 (km/s)^2 (right), free t_f , EME2000 RF.

Many T-C solutions of the free C_3 case assume the two-burn T-C-T-C structure when constrained to $C_3 = 0.2 \text{ (km/s)}^2$, especially those belonging to the second family. Moreover, a peculiarity to be observed, clearly shown in the corresponding Tables 5 and 6, is that low-energy and high-energy fixed solutions, for selected studies, tend to invert the optimal thrust structure from 2 to 4 phases and vice versa.

Table 5. EML2 escapes performance—fixed $C_3 = 0.2 \text{ (km/s)}^2$, free t_f .

C	f	p	$\eta_{SP,u}$	$\eta_{SP,v}$	$\overline{\eta_{SP}}$	ΔV m/s	t_f days
1	I	2	0.702	−0.274	0.214	46.297	78.59
2	I	4	0.711	−0.195	0.258	66.200	75.12
3	II	4	0.190	0.542	0.366	73.777	88.05
3	III	2	0.715	−0.241	0.237	17.354	80.81
4	III	2	0.678	−0.295	0.192	39.099	73.93
5	I	2	0.659	−0.314	0.172	49.933	78.43

Table 6. EML2 escapes performance—fixed $C_3 = 0.5 \text{ (km/s)}^2$, free t_f .

C	f	p	$\eta_{SP,u}$	$\eta_{SP,v}$	$\overline{\eta_{SP}}$	ΔV m/s	t_f days
1	I	4	0.695	0.541	0.618	74.853	75.01
2	I	2	0.632	0.301	0.467	147.635	61.40
3	I	2	0.449	0.713	0.581	19.934	72.74
4	I	2	0.654	0.308	0.481	77.468	62.79
5	I	4	0.683	0.539	0.611	64.702	76.59

Figure 19 shows that solutions group themselves towards favorable values of the solar perturbation. For the $C_3 = 0.2 \text{ (km/s)}^2$ scenario on the left, some trajectories are shown; case 1 and case 2, from the family I, have high positive values of the solar tangential perturbation, while cases 3 and 4 from family III overlap towards the same scenario, in the opposite heliocentric direction. The corresponding family II solution of case 3, which is a two-burn trajectory, exploits more consistently the radial component and uses more propellant to achieve the escape. The $C_3 = 0.5 \text{ (km/s)}^2$ case, on the other hand, has trajectories that move towards positive influences of the tangential solar perturbation, with cases 1, 2, and 5 that favor the Sun in the third quadrant and cases 3 and 4 in the first quadrant. Only case 2, depicted in Figure 18 (right), which departs 90° later than case 1 but

converges to the same final point, needs to perform a longer burn at the beginning to align the outward trajectory to the correct direction.

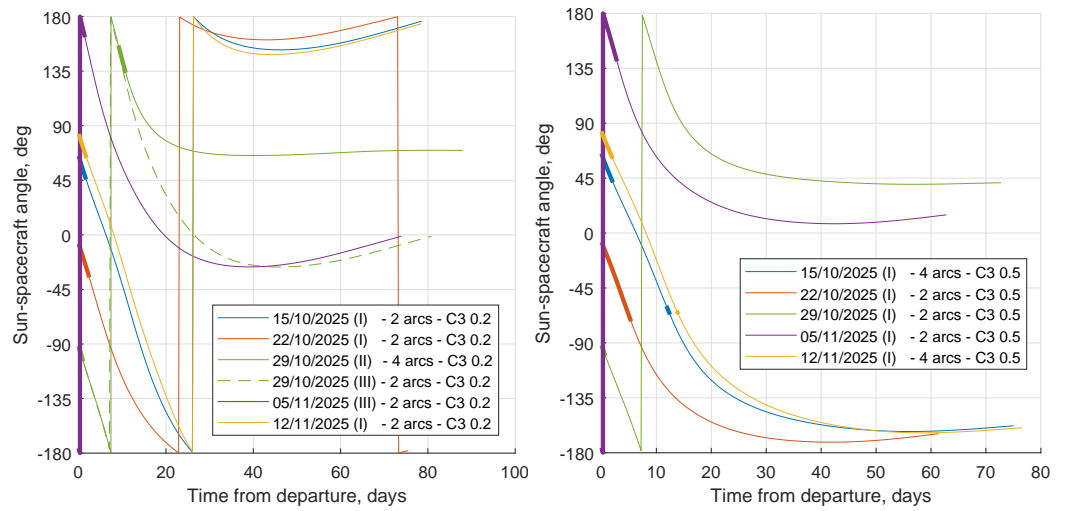


Figure 19. Time evolution of Sun–spacecraft relative angle for all EML2 solutions—fixed $C_3 = 0.2 \text{ (km/s)}^2$ (left), 0.5 (km/s)^2 (right), free t_f .

Figure 20 shows two sample cases, 2 and 3, selected to show low- and high-energy trajectories that must either increase or decrease the energy to achieve the fixed energy counterparts. In particular, case 2 from the free energy scenario has a very low final energy, whereas case 3 has a very high one. The four-arc solution for case 2 slightly reduces its duration while increasing the first thrust phase to comply with the final energy increase and keep similar $\Delta\theta$ during the escape. This action eliminates the second burn making it a T–C trajectory. When forced to have the higher final energy, the optimal strategy keeps reducing the overall duration to escape, while increasing the thrust phase length; indeed, the solution forces the relative angle to stay in the third quadrant between -135° and -180° , where the solar perturbation acts more favorably.

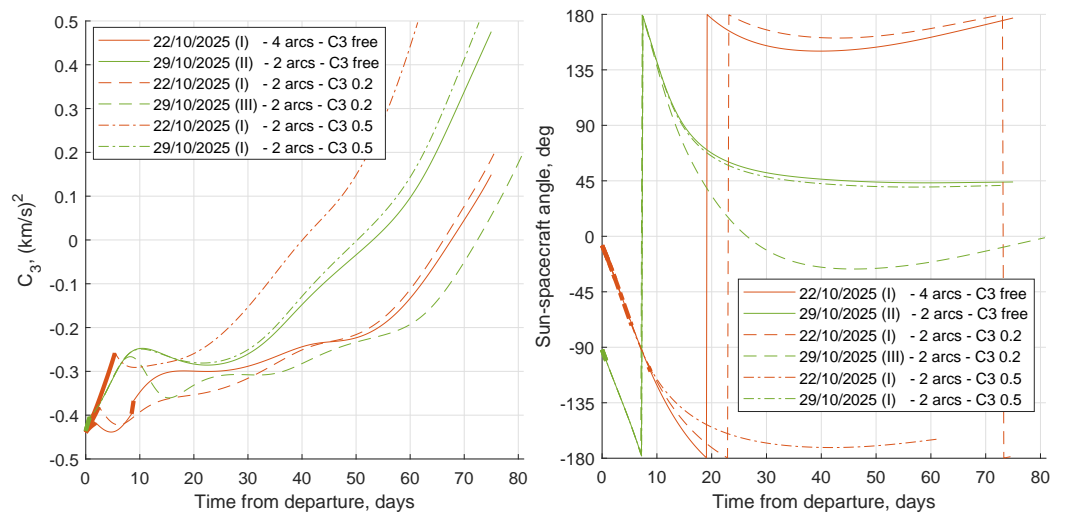


Figure 20. Spacecraft energy over time (left) and Sun–spacecraft relative angle (right) for selected EML2 escape dates—comparison between free and fixed final C_3 .

With an opposite behavior, the single burn solution in the scenario with free final energy for case 3 has to reduce its overall energy to achieve the required lower C_3 . This increases the overall length of the trajectory with a strong reduction in the first burn phase, showing that the optimal strategy relies mainly on the solar perturbation to achieve the

desired energy. Indeed, the majority of the escape, after the initial 30 days, remains in a region in which the Sun perturbation has a negative effect, retarding the energy increase.

6. Applications

The results obtained in this article represent a preliminary approach to the indirect optimization of escape trajectories from Lagrangian points. On the one hand, they can be used as tentative solutions for the indirect optimization of escape transfers from practical orbits around/in the vicinity of Lagrangian points. On the other hand, these escape transfers can be coupled to the analysis of interplanetary legs for the design of missions aimed at near-earth asteroids.

A complete analysis of escape transfers for different orbits around SEL2 and EML2, considering the influence of orbit characteristics, departure point and date, etc., is beyond the scope of the present article. Only high-fidelity Lyapunov orbits around SEL2 are considered as examples. Departure occurs on October 15 2025, from the orbit intersection with the Sun-Earth L2 line, i.e., the x -axis of the Sun-Earth synodic frame, (between Earth and L2) and 90-day escape transfers with free C_3 are considered. The initial orbits are characterized by their Jacobi constant and start from the x -axis at about 200×10^3 km, 400×10^3 km, and 800×10^3 km from L2. The solution starting from L2 is used as a tentative solution for departures from Lyapunov orbits and convergence is readily obtained. It is worth noting that the new solutions can, in turn, be used as tentative guesses for other studies (e.g., for the optimization of departure point and/or escape duration). Table 7 and Figure 21 compare the escape trajectories from L2 and from the three Lyapunov orbits. The escape transfers show similar propulsive requirements. Escape C_3 tends to be smaller for the larger Lyapunov orbits; this value is however sensibly influenced by the escape duration and different control structures (e.g., a second thrust arc) could eventually become optimal for constrained C_3 values.

Table 7. Comparison of escapes performance for escape from L2 and Lyapunov orbits—free C_3 fixed t_f 90 days.

Departure	JC (km/s) ²	ΔV m/s	$C_{3,f}$ (km/s) ²
L2	3.000887	30.676	0.1833
Lyapunov 1	3.000880	37.607	0.1298
Lyapunov 2	3.000858	34.916	0.0836
Lyapunov 3	3.000776	32.869	0.0263

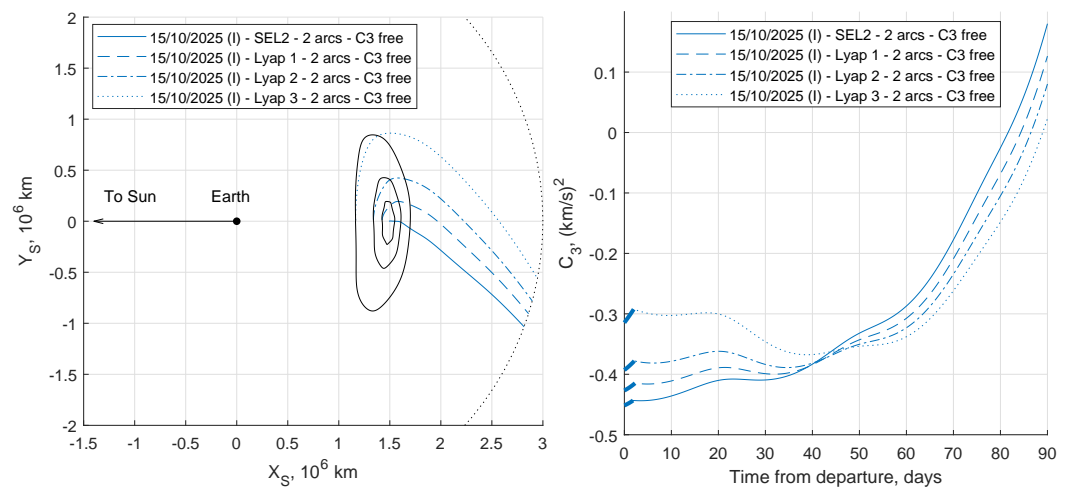


Figure 21. Performance comparison for escapes from L2 and Lyapunov orbits—Sun-Earth rotating RF (left), energy over time (right)—free C_3 , fixed t_f 90 days.

The preliminary design of interplanetary trajectories usually starts from the patched-conic approximation. The analysis of escape maneuvers and heliocentric leg are often treated separately at an initial state, and the results are then coupled for a high-fidelity analysis of the complete transfers. This approach was, for instance, used to design the ARRM mission [18,35]. In a similar way, the results for the L2 escape obtained in this article can be useful to design interplanetary transfers. Only the 90-day escape from SEL2 with free C_3 and departure on 15 October 2025, is again taken as an example. The small C_3 value suggests that this trajectory can be fit for transfers to NEAs and a set of 75 asteroids considered in previous works [36,37] is explored. The escape direction has a specific orientation in the Sun-Earth system (see Figure 6), which should be suited to reach only the targets that require a similar orbit correction at the selected departure.

The interplanetary leg with two-body dynamics is optimized with different initial conditions to highlight the effect of the actual escape maneuver on the overall performance. Departure from Earth's position with $C_3 = 0$ (km/s)² on 13 January 2026 (i.e., 15 October 2025, +90 days) is assumed as the reference trajectory. The length of the heliocentric transfer to rendezvous with the asteroid is 3 years. The reference solutions are compared to trajectories with departure from the actual heliocentric position and velocity corresponding to the 90-day escape trajectory departing 15 October 2025.

In this example, escape from L2 improves the reference trajectory for 21 out of 75 available targets. Propellant budget comparison for these solutions is shown in Table 8, ordered by percentage propellant saving. Note that 8 out of the first 10 asteroids have perihelion in the first quadrant, where the perihelion of the heliocentric orbit at escape lies; the required change in orbital elements is reduced, explaining the saving. The optimal rendezvous transfer is also influenced by a phasing constraint, which may require different orbit adjustments; therefore, this general observation has exceptions.

Table 8. SEL2 escapes—asteroid rendezvous propellant mass requirements.

Asteroid	Reference kg	90-Day Escape kg	% Saving
2016 TB57	111.1	76.5	31.2
2013 XY20	82.4	59.7	27.5
2016 CF137	110.5	82.5	25.3
2017 BF29	88.9	66.8	24.8
2011 AA37	64.1	53.1	17.2
2012 BA35	185.7	152.8	17.7
2007 DD	185.3	152.6	17.6
2017 HK1	106.8	88.6	17.1
2015 TJ1	86.0	73.6	14.4
2014 EK24	80.0	69.6	13.0
2017 HZ4	123.4	108.9	11.8
2006 FH36	143.9	126.8	11.9
2015 BM510	88.6	78.8	11.0
2010 HA	76.5	68.3	10.8
2009 OS5	77.7	69.4	10.7
1996 XB27	70.3	63.6	9.6
2016 FY2	106.3	97.0	8.8
2015 VV	75.2	70.0	6.9
2001 QJ142	82.7	79.6	3.8
2013 EM89	66.3	64.9	2.1
2013 RV9	103.7	102.3	1.4

7. Conclusions

An indirect method has been used for the optimization of EP escape trajectories from either Sun-Earth or Earth-Moon L2. Even in the presence of complex dynamics and nonlinear effects, the method proves to be fast and reliable, thanks to the peculiar treatment of the thrust magnitude. The complexity of motion dynamics makes convergence difficult and causes the existence of local optima. The techniques to obtain converged solutions introduced in this article allow one to efficiently explore the solution space and identify local and global minima of the propellant consumption.

Escape from Sun-Earth L2 is relatively simple, as proper selection of time of flight and departure date can guarantee suitable escape conditions with extremely low propulsive requirements. Escape from Earth-Moon L2 shows the complex interaction that the relative positions of the Moon and the Sun produce on the escape trajectory. On the one hand, the departure date determines the direction of the escape hyperbola; on the other hand, it influences the switching structure as the spacecraft tries to maximize the effect of solar gravity. Privileged escape directions are easily recognized.

The results obtained in this paper offer a good understanding of the main driving effects that characterize escape trajectories from L2. This analysis provides the basis for consideration of different departure conditions. Departure from Lyapunov orbits is straightforward using escape trajectories from L2 as tentative guess. Extension to other cases—such as those that correspond to an NRHO in the Earth-Moon system or a Lissajous orbit around Sun-Earth L2—can then be pursued using continuation approaches to modify the initial orbit.

Indirect optimization is computationally fast and escape trajectories can be rapidly evaluated to build a database of escape conditions/cost. These results can in turn be coupled to the optimization of the heliocentric leg for the preliminary design of interplanetary missions, providing a more accurate evaluation of the propulsive requirements.

Author Contributions: L.M. and L.C. contributed equally to the manuscript. All authors have read and agreed to the published version of the manuscript.

Funding: This research received no external funding.

Data Availability Statement: Not applicable.

Conflicts of Interest: The authors declare no conflict of interest.

Abbreviations

The following abbreviations are used in this manuscript:

BVP	boundary value problem
DSG	Deep Space Gateway
EME2000	Earth Mean Equator and Equinox of Epoch J2000
EML2	Earth-Moon Lagrangian point 2
EP	electric propulsion
ICRF	International Celestial Reference Frame
LOP-G	Lunar Orbital Platform Gateway
LP(s)	Lagrangian point(s)
MOID	minimum orbit intersection distance
NEA(s)	near-earth asteroid(s)
NRHO(s)	near rectilinear halo orbit(s)
PMP	Pontryagin's maximum principle
RF	reference frame
SEL2	Sun-Earth Lagrangian point 2
SOI	sphere of influence
SRP	solar radiation pressure

Nomenclature

a	semi-major axis, AU
a	perturbing acceleration
c	effective exhaust velocity, km/s
C_3	characteristic energy, (km/s) ²
H	Hamiltonian
m	mass, kg
p	radiation pressure, N/m ²
P	Power, W
q	unknowns tentative values
r	radius
R	relative distance
S_F	switching function
t	time
T	thrust, N
u	velocity, radial component, km/s
\hat{u}	unit vector
v	velocity, tangential component, km/s
V	velocity, km/s
w	velocity, out-of-plane component, km/s
η	normalized solar perturbation contribution
η_R	reflectivity
η_T	thruster global efficiency
$\Delta\theta$	Sun–spacecraft relative angular difference, deg
θ	right ascension, deg
λ	adjoint variables
μ	specific gravitational parameter, km ³ /s ²
ξ	proportionality term
φ	declination, deg
χ	error on boundary conditions

Subscripts

0	initial
f	final
i	radial direction
j	tangential direction
J	non-sphericity perturbation
ℓ	lunar
lsg	lunisolar gravity perturbation
s	sun
srp	solar radiation pressure perturbation

Appendix A. Euler–Lagrange Equations

The system of Equations (5)–(11) is used to write the Hamiltonian in scalar form as $H = \sum \lambda_x \dot{x}$. Each adjoint variable λ_x is associated with the generic state variable $x = r, \vartheta, \varphi, u, v, w, m$. A compact expression of the Euler–Lagrange Equations is $\dot{\lambda}_x = -\partial H / \partial x$. When carrying out the derivatives, one should note that the state variables appear explicitly in Equations (5)–(11), but some state variables also influence the additional accelerations and the thrust magnitude.

Third-body position components in the spacecraft-centered topocentric frame (subscript $b = s, l$ for Sun and Moon) are written as

$$(r_b)_u = x_b \cos \vartheta \cos \varphi + y_b \sin \vartheta \cos \varphi + z_b \sin \varphi \quad (\text{A1})$$

$$(r_b)_v = -x_b \sin \vartheta + y_b \cos \vartheta \quad (\text{A2})$$

$$(r_b)_w = -x_b \cos \vartheta \sin \varphi - y_b \sin \vartheta \sin \varphi + z_b \cos \varphi \quad (\text{A3})$$

(third-body Cartesian coordinates are obtained by JPL’s ephemerides). The space position with respect to the third body is written as $\mathbf{R}_b = \mathbf{r} - \mathbf{r}_b$ and the gravitational effect becomes (same formal expression for Sun and Moon) the following:

$$(a_b)_u = (\mu_b/R_b^3)[(r_b)_u - r] - (\mu_b/r_b^3)(r_b)_u \tag{A4}$$

$$(a_b)_v = (\mu_b/R_b^3)(r_b)_v - (\mu_b/r_b^3)(r_b)_v \tag{A5}$$

$$(a_b)_w = (\mu_b/R_b^3)(r_b)_w - (\mu_b/r_b^3)(r_b)_w \tag{A6}$$

with dependence on r, ϑ and φ . The spacecraft distance from the Sun or from the Moon is $R_b = \sqrt{[r - (r_b)_u]^2 + (r_b)_v^2 + (r_b)_w^2}$.

Solar radiation pressure is similar to solar gravity, but also depends on m . The photon pressure at 1 AU from the sun is $p = 4.55682 \times 10^{-6} \text{ N/m}^2$ Assuming reflectivity $\eta_R = 0.7$, the acceleration on a spherical body of mass m and surface S at a distance from the Sun R_s is

$$(a_{srp})_u = -(1 + \eta_R) \left(p/R_s^3 \right) (S/m) [(r_s)_u - r] \tag{A7}$$

$$(a_{srp})_v = -(1 + \eta_R) \left(p/R_s^3 \right) (S/m) (r_s)_v \tag{A8}$$

$$(a_{srp})_w = -(1 + \eta_R) \left(p/R_s^3 \right) (S/m) (r_s)_w \tag{A9}$$

and is again function of r, ϑ , and φ , but also depends on the mass, m .

Earth’ potential is written as follows:

$$V = -\mu_E/r \left\{ 1 + \sum_{n=2}^N \left(\frac{r_E}{r} \right)^n \sum_{m=0}^n [C_{nm} \cos(m\vartheta_{Lo}) + S_{nm} \sin(m\vartheta_{Lo})] P_{nm} \sin(\varphi) \right\} \tag{A10}$$

The terrestrial latitude coincides with declination φ as nutation is neglected. The terrestrial longitude, ϑ_{Lo} , is obtained as $\vartheta_{Lo} = \vartheta - \vartheta_G$, with Greenwich right ascension at time, t , given by $\vartheta_G = \vartheta_{Gref} + \omega_E(t - t_{ref})$. The reference time t_{ref} is 1/1/2000 12:00 UT (51,544.5 MJD) and $\vartheta_{G0} = 280.46061837504 \text{ deg}$; ω_E is evaluated assuming the sidereal day equal to 86,164.098903690351 s (no precession is considered). The perturbing acceleration due to Earth’s non-sphericity is the gradient of $\Phi = V + \mu_E/r$, and its components in the topocentric frame are thus evaluated as follows:

$$(a_J)_u = \partial\Phi/\partial r \tag{A11}$$

$$(a_J)_v = (\partial\Phi/\partial\vartheta)/(r \cos \varphi) \tag{A12}$$

$$(a_J)_w = (\partial\Phi/\partial\varphi)/r \tag{A13}$$

Derivation with respect to r and ϑ is straightforward; derivatives with respect to φ require the derivatives of the associated Legendre functions, which are obtained recursively, exploiting the properties of Legendre polynomials. The summed acceleration components are compactly written as $a_j = (a_s)_j + (a_\ell)_j + (a_{srp})_j + (a_J)_j$ with $j = u, v, w$.

Finally the thrust magnitude is written as the reference thrust at 1 AU divided by the squared distance from the Sun in AU, that is $T = T_1/R_s^2$ and also depends on r, ϑ , and φ . The Euler–Lagrange equations become

$$\begin{aligned} \dot{\lambda}_r = & \frac{1}{r^2} \left[\lambda_\theta \frac{v}{\cos \phi} + \lambda_\phi w + \lambda_u \left(-\frac{2\mu}{r} + v^2 + w^2 \right) + \lambda_v (-uv + vw \tan \phi) \right. \\ & \left. + \lambda_w (-uw - v^2 \tan \phi) \right] - \lambda_u \frac{\partial a_u}{\partial r} - \lambda_v \frac{\partial a_v}{\partial r} - \lambda_w \frac{\partial a_w}{\partial r} - S_F \frac{\partial T}{\partial r} \end{aligned} \quad (A14)$$

$$\dot{\lambda}_\theta = -\lambda_u \frac{\partial a_u}{\partial \theta} - \lambda_v \frac{\partial a_v}{\partial \theta} - \lambda_w \frac{\partial a_w}{\partial \theta} + S_F \frac{\partial T}{\partial \theta} \quad (A15)$$

$$\begin{aligned} \dot{\lambda}_\phi = & \frac{1}{r \cos^2 \phi} \left(-\lambda_\theta v \sin \phi - \lambda_v vw + \lambda_w v^2 \right) \\ & - \lambda_u \frac{\partial a_u}{\partial \phi} - \lambda_v \frac{\partial a_v}{\partial \phi} - \lambda_w \frac{\partial a_w}{\partial \phi} + S_F \frac{\partial T}{\partial \phi} \end{aligned} \quad (A16)$$

$$\dot{\lambda}_u = \frac{1}{r} (-\lambda_r r + \lambda_v v s. + \lambda_w w) \quad (A17)$$

$$\dot{\lambda}_v = \frac{1}{r} \left[-\lambda_\theta \frac{1}{\cos \phi} - 2\lambda_u v + \lambda_v (u - w \tan \phi) + 2\lambda_w v s. \tan \phi \right] \quad (A18)$$

$$\dot{\lambda}_w = \frac{1}{r} (-\lambda_\phi - 2\lambda_u w - \lambda_v v s. \tan \phi + \lambda_w u) \quad (A19)$$

$$\dot{\lambda}_m = \frac{T}{m^2} \lambda_V - \lambda_u \frac{\partial a_u}{\partial m} - \lambda_v \frac{\partial a_v}{\partial m} - \lambda_w \frac{\partial a_w}{\partial m} \quad (A20)$$

References

- Vallado, D.A. *Fundamentals of Astrodynamics and Applications*, 4th ed.; Space Technology Library, Microcosm Press: Cleveland, OH, USA, 2013; pp. 122–129.
- SOHO (Solar and Heliospheric Observatory). Available online: <https://eoportal.org/web/eoportal/satellite-missions/content/-/article/soho> (accessed on 27 February 2022).
- WIND (Interplanetary Physics Laboratory). Available online: <https://wind.nasa.gov/> (accessed on 27 February 2022).
- Herschel Space Telescope. Available online: https://www.esa.int/Enabling_Support/Operations/Herschel (accessed on 27 February 2022).
- Planck Space Telescope. Available online: https://www.esa.int/Enabling_Support/Operations/Planck (accessed on 27 February 2022).
- The DSCOVR: Deep Space Climate Observatory. Available online: <https://www.nesdis.noaa.gov/current-satellite-missions/currently-flying/dscovr-deep-space-climate-observatory> (accessed on 27 February 2022).
- LPF (LISA Pathfinder) Mission. Available online: <https://directory.eoportal.org/web/eoportal/satellite-missions/1/lisa-pathfinder> (accessed on 27 February 2022).
- The “No Name” Space Weather Mission. Available online: https://www.esa.int/Safety_Security/The_no_name_space_weather_mission (accessed on 27 February 2022).
- European Space Agency. The PLATO Mission. 2014. Available online: <https://www.cosmos.esa.int/web/plato> (accessed on 27 February 2022).
- De Iuliis, A.; Mascolo, L.; De Santi, L.; Casalino, L. Asteroid Rendezvous Missions with Departure From Earth-Sun L4 and L5. In Proceedings of the 2020 AAS/AIAA Astrodynamics Specialist Conference, South Lake Tahoe, CA, USA, 9–12 August 2020.
- Lunar Gateway of NASA’s Artemis Program. Available online: <https://directory.eoportal.org/web/eoportal/satellite-missions/1/lunar-gateway> (accessed on 27 February 2022).
- Fuller, S.; Lehnhardt, E.; Zaid, C.; Halloran, K. Gateway Program Status and Overview. In Proceedings of the 72nd International Astronautical Congress, Dubai, United Arab Emirates, 25–29 October 2021; Iafastro; IAC-21, A3, 2B, 13, x66240.
- National Aeronautics and Space Administration: ARTEMIS PLAN. NASA’s Lunar Exploration Program Overview. Technical Report NP-2020-05-2853-HQ. Available online: https://www.nasa.gov/sites/default/files/atoms/files/artemis_plan-20200921.pdf (accessed on 27 February 2022).
- Lee, D.E. *White Paper: Gateway Destination Orbit Model: A Continuous 15 Year NRHO Reference Trajectory*; Technical Report JSC-E-DAA-TN72594, Document ID: 20190030294; National Aeronautics and Space Administration, NASA Johnson Space Center: Houston, TX, USA, 2019.
- Simeoni, F.; Casalino, L.; Zavoli, A.; Colasurdo, G. Indirect Optimization of Satellite Deployment into a Highly Elliptic Orbit. *Int. J. Aerosp. Eng.* **2012**, *2012*, 152683. [CrossRef]
- Mascolo, L.; Casalino, L. Escape Trajectories from Lagrangian Points with Electric Propulsion. In Proceedings of the 2021 31st AAS/AIAA Space Flight Mechanics Meeting, Charlotte, NC, USA, 1–4 February 2021.
- Colasurdo, G.; Casalino, L. Tentative Solutions for Indirect Optimization of Spacecraft Trajectories In *Space Engineering. Springer Optimization and Its Applications*; Fasano, G., Pinter, J.D., Eds.; Springer: Cham, Switzerland, 2017; Volume 114. [CrossRef]
- Casalino L.; Lantoine, G. Design Of Lunar-Gravity-Assisted Escape Trajectories. *J. Astronaut. Sci.* **2020**, *67*, 1374–1390. [CrossRef]

19. Matsumoto, M. Deep Space Transportation System Using the Sun-Earth L2 Point. In Proceedings of the 20th International Symposium on Space Flight Dynamics, Annapolis, MA, USA, 24–28 September 2007.
20. Bernelli Zazzera, F.; Topputo, F.; Massari, M. *Assessment of Mission Design Including Utilization of Libration Points and Weak Stability Boundaries*; Ariadna ID: 03/4103, C/N 18147/04/NL/MV, ACT (ESTEC); ESA Advanced Concept Team: Noordwijk, The Netherlands, 2004.
21. Tanaka, K.; Kawaguchi, J. Escape Trajectories from the L2 Point of the Earth-Moon System. *Jpn. Soc. Aeronaut. Space Sci.* **2014**, *57*, 238–244. [[CrossRef](#)]
22. Jet Propulsion Laboratory—Solar System Dynamics Branch, JPL Planetary and Lunar Ephemerides, Export Information 21 December 2020. Available online: https://ssd.jpl.nasa.gov/?planet_eph_export (accessed on 27 February 2022).
23. Bryson, A.E.; Ho, Y.C. *Applied Optimal Control*, 1st ed.; Hemisphere Publications: New York, NY, USA, 1975; pp. 42–89.
24. Casalino, L.; Colasurdo, G.; Pastrone, D. Optimal Low-Thrust Escape Trajectories Using Gravity Assist. *J. Guid. Control. Dyn.* **1999**, *22*, 637–642. [[CrossRef](#)]
25. Bertrand, R.; Epenoy, R. New smoothing techniques for solving bang-bang optimal control problems—Numerical results and statistical interpretation. *Optim. Control Appl. Methods* **2002**, 171–197. [[CrossRef](#)]
26. Silva, C.; Trélat, E. Smooth Regularization of Bang-Bang Optimal Control Problems. *IEEE Trans. Autom. Control* **2010**, *55*, 2488–2499. [[CrossRef](#)]
27. Taheri, E.; Junkins, J.L. Generic Smoothing for Optimal Bang-Off-Bang Spacecraft Maneuvers. *J. Guid. Control. Dyn.* **2018**, *41*, 2467–2472. [[CrossRef](#)]
28. Gao, Z.; Baoyin, H. Using Homotopy Method to Solve Bang–Bang Optimal Control Problems. *Optim. Simul. Control* **2013**, 243–256. [[CrossRef](#)]
29. Zhu, Z.; Gan, Q.; Yang, X.; Gao, Y. Solving fuel-optimal low-thrust orbital transfers with bang-bang control using a novel continuation technique. *Acta Astronaut.* **2017**, *137*, 98–113. [[CrossRef](#)]
30. Mall, K.; Grant, M.J.; Taheri, E. Uniform Trigonometrization Method for Optimal Control Problems with Control and State Constraints. *J. Spacecr. Rocket.* **2020**, *57*, 995–1007. [[CrossRef](#)]
31. Antony, T.; Grant, M.J. Path Constraint Regularization in Optimal Control Problems using Saturation Functions. In Proceedings of the 2018 AIAA Atmospheric Flight Mechanics Conference, Kissimmee, FL, USA, 8–12 January 2018; AIAA 2018-0018. [[CrossRef](#)]
32. ESA Science & Technology. Available online: <https://sci.esa.int/web/cosmic-vision/-/61416-esa-s-new-mission-to-intercept-a-comet> (accessed on 27 February 2022).
33. eoPortal EQUULEUS and OMOTENASHI. Available online: <https://directory.eoportal.org/web/eoportal/satellite-missions/e/equuleus> (accessed on 27 February 2022).
34. Funase, R.; Ikari, S.; Miyoshi, K.; Kawabata, Y.; Nakajima, S.; Nomura, S.; Funabiki, N.; Ishikawa, A.; Kakihara, K.; Matsushita, S.; et al. Mission to Earth-Moon Lagrange Point by a 6U CubeSat: EQUULEUS. *IEEE Aerosp. Electron. Syst. Mag.* **2021**, *35*, 30–55. [[CrossRef](#)]
35. Merrill, R.G.; Ou, M.; Vavrina, M.A.; Jones, C.A.; Englander, J. Interplanetary Trajectory Design for the Asteroid Robotic Redirect Mission Alternate Approach Trade Study. In Proceedings of the AIAA/AAS Astrodynamics Specialist Conference, San Diego, CA, USA, 4–7 August 2014; Paper AIAA 2014-4457. [[CrossRef](#)]
36. Mereta, A.; Izzo, D. Target Selection for a Small Low-Thrust Mission to Near-Earth asteroids. *Astrodynamics* **2018**, *2*, 249–263. [[CrossRef](#)]
37. Mascolo, L.; De Iuliis, A.; Casalino, L. Fast and Accurate Estimation of Fuel-Optimal Trajectories to Near-Earth Asteroids. *Acta Astronaut.* **2021**, *188*, 49–56. [[CrossRef](#)]